7th International Conference on Innovation in High Performance Sailing Yachts and Wind Assisted Ships.
InnovSail 2026, Gothenburg, Sweden, 3-5 June 2026.

High-Performance Stringer-Stiffened Composite Hull Structures under Slamming Loads: The Effects of Hydroelasticity and Non-Uniform Pressure Loads

Connor Pearson
University of Auckland, NZ, connor.pearson@auckland.ac.nz

Mark Battley
University of Auckland, NZ.

Jean-Baptiste R. G. Souppez
Birmingham City University, UK.

Tom Allen
University of Auckland, NZ.

Abstract. Water impacts form a critical load for the outer hull panels of small high-speed marine craft. These result in highly localised non-uniform pressure pulse, which propagates along a hull panel as it is immersed. While slamming is multi-functional and stochastic, the severity of the impact is primarily a function of the vertical impact velocity, and angle between the panel and free surface, known as the deadrise. Due to the complexities of water impacts, design standards —such as those defined in ISO-12215-5— recommend that hull panels are designed based on a static uniform pressure. However, these are unable to produce the same strain state as a water impact, leading to a disconnect between real-world and as-designed performance.

This study addresses this gap using hydroelastic simulations of the slamming of a stringer-stiffened panel typical of current generations of ocean-going racing yachts, and makes suggestions to improve the analysis of such structures during the design process. Results indicate that the structural response of such panels is dependent on the location of the pressure pulse and the effects of hydroelasticity, which are not accounted for when using a uniform pressure. The Authors recommend that design processes may be improved by statically solving for key instants during the water impact using analytically derived non-uniform pressures. Such a method reduces the discrepancy between real-world and as-designed laminate strains to only 33.6%, compared to the 65.8% reported when using a uniform pressure load, representing a significant improvement over the current design standards.

Keywords: Stringer-stiffened composite panels; Marine hull structures; Slamming loads; Constant velocity water impacts; Hat/Omega stringers.

NOMENCLATURE

B	Wedge or panel beam [m]
c	Location of the contact point along x ($0.5\pi x$) [m]
c_s	Speed of sound through the fluid [m s^{-1}]
F	Vertical impact force [N]
L	Wedge or panel span (if the problem is three-dimensional) [m]
L_{WL}	Length of waterline at rest [m]
P	Applied pressure [Pa]
t	Time [s]
ΔP	Difference from atmospheric pressure [Pa]
V	Craft velocity [kn]
V_v	Instantaneous vertical impact velocity [m s^{-1}]
x	Horizontal distance from the keel [m]
x_o	Distance from x-axis origin [mm]
y_o	Distance from y-axis origin [mm]
β_r	Deadrise angle [rad]
δ	Slamming spray jet thickness [m]
ρ_w	Density of the water [kg m^{-3}]
τ	Numerically determined solution parameter based on the spray jet thickness, δ [-]
C	Capping strains
CC	Chine-side cove-former boundary strains
CFRP	Carbon-Fibre Reinforced Polymer
CFD	Computational Fluid Dynamics
CK	Keel-side cove-former boundary strains
F	Flexible impact
FEA	Finite Element Analysis
ISO	International Organisation for Standardisation
MHRIC	Modified High-Resolution Interface Capturing
PCC200	200 gsm Twill-weave Carbon Prepreg
PCU150	150 gsm Unidirectional Carbon Prepreg
PRESTO	PREssure STaggering Option
SIMPLEC	Semi-Implicit Method for Pressure Linked Equations - Consistent
R	Rigid impact
R-D	Dynamic Rigid impact
R-S	Quasi-static Rigid impact
S	Skin strains
SM	Standard Modulus
SSCP	Stringer-Stiffened Composite Panel
SSTS	Servo-hydraulic Slam Testing System
VOF	Volume Of Fluid
WC	Chine-side web strains
WK	Keel-side web strains

1 INTRODUCTION

Water impacts form a critical load for the outer hull panels of small high-speed marine craft, defined by the International Organisation for Standardisation (ISO) as a hull length up to 24 m and a maximum speed of $V \geq 5\sqrt{L_{WL}}$ (ISO, 2019). Such impacts apply a high-magnitude, localised, and propagat-

ing out-of-plane hydrodynamic pressure to the wetted surface of the hull panels, forming a complex and multi-faceted load case that is difficult to design against. These difficulties are attributed to the stochastic nature of in-service impacts (Rosén et al., 2007), the costs of the experimental testing (Qi, 2018), and the infeasibility of complex numerical simulations during the design process (ISO, 2019). Further complications are introduced by hydroelasticity, which results in a coupling and feedback loop between the structural and fluid response; the deformations of the panel influence and modify the applied pressure distribution.

Current structural design standards —such as ISO 12215-5 (ISO, 2019)— reduce this complexity through the assumption of static uniform pressure loads, leading to a disconnect between real-world and as-designed performance. Such standards are based on a series of foundational studies conducted in the 1960s and 1970s (Heller and Jasper, 1960; Allen et al., 1978) and may no longer be applicable to small high-speed marine craft, which are progressively constructed of advanced composite materials and structures, nor the increasingly higher speeds and rough conditions they are operated in (ISO, 2019; Souppez, 2018). Without a comprehensive investigation to determine validity, structures designed to these standards may be potentially unsafe or failure-prone, leading to the loss of craft or life.

Recent design trends have seen the increased use of stiffened single skin structures for the bottom hull panels of high-performance marine craft, due higher specific strengths and stiffnesses and the removal of core-shear failure mechanisms found in sandwich structures (Charca and Shafiq, 2011; Allen and Battley, 2015; Lorimer and Allen, 2022). Such structures are defined as Stringer-Stiffened Composite Panels (SSCPs). Significant attention has been given to the analysis of composite sandwich (Breder, 2005; Battley et al., 2009; Charca and Shafiq, 2011; Charca et al., 2009; Allen, 2013; Stenius et al., 2013; Allen and Battley, 2015) and stiffened metallic panels (Xie et al., 2018; Chen et al., 2023; Hosseinzadeh et al., 2023a; Hosseinzadeh et al., 2023b), but the behaviour of SSCPs during water impacts has not been widely studied. Pearson et al. (2024) and Pearson et al. (2026c) found that during the water impact of an SSCP, peak strains are heavily dependant on the orientation and propagation direction of the pressure pulse, the structural response of the various SSCP regions sequential and independent (Regions located closer to the keel are loaded first, and this has very little effect on the subsequent response of upstream regions), and hydroelasticity results in a reduction in the severity of a water impact. Critical strains were identified as the lateral skin at the midspan, longitudinal capping at the midspan, and web shear near the bulkhead. However, the mechanisms of the hydroelasticity are poorly understood, and there was yet to be a comprehensive examination of the differences between uniform and slamming pressures on the structural response of SSCPs.

This study addresses this lack of understanding between real-world and as-designed performance of water impacting hull panels using a two-way coupled Computational Fluid Dynamics - Finite Element Analysis (CFD-FEA) analysis methodology, focusing on stringer-stiffened composite panels found on recent generations of IMOCA60 ocean-racing yachts. This represents one of the first studies to investigate the structural response of SSCPs in water impacts Various types of impact are simulated, from a full flexible scenario, a rigid scenario, and an equivalent uniform pressure load. In this work, a rigid impact refers to the lack of hydroelastic coupling between the fluid and structural responses; SSCP deformations are not considered by the fluid solver, which treats the impacting structure as a rigid panel. In a flexible impact, hydroelastic coupling and SSCP deformations are considered by the fluid solver. Experimental tests are inherently considered as flexible impacts. Peak strains from each impact scenario are compared, and the conclusions are used to suggest new analysis techniques that may be used during the design process of the outer hull panels of high-performance marine craft.

2 METHODOLOGY

2.1 Outline of Slamming Specimen and Investigative Scope

The SSCPs examined in this work were derived from recent generations of IMOCA60 ocean-racing yachts. The SSCP specimens featured an omega-type stringer constructed of Carbon-Fibre Reinforced Polymer (CFRP) prepreg with an internal foam former. Hat- and omega-type stringers are popular in the marine industry as they can easily be incorporated into the construction process. This cross-sectional profile can be formed by laminating over a machined foam former which remains within the structure. This eliminates the need for complex secondary moulds or co-curing regimes, which are difficult to achieve in the continuously-varying three-dimensional hull form of a custom, one-off, high-performance racing yacht. CFRP laminates were comprised of 150 gsm Standard Modulus (SM) carbon unidirectional prepreg (PCU150) and 200 gsm SM carbon twill prepreg (PCC200) manufactured by Hankuk Ltd. The cross-sectional geometry and laminates of the SSCPs tested in this study are illustrated in Fig. 1, while the final 1030 x 675 mm slamming specimen is displayed in Fig. 2. Longitudinal and lateral directions have been defined along the length and across the width of the stringers. More information on the design of the SSCP slamming specimen can be found in Pearson et al. (2026c), where the findings of an experimental study of this same specimen are published. This experimental study involved driven water impacts of an SSCP at 0.5–8.0 m s^{-1} using the novel Servo-hydraulic Slam Testing System (SSTS) (Battley and Allen, 2012).

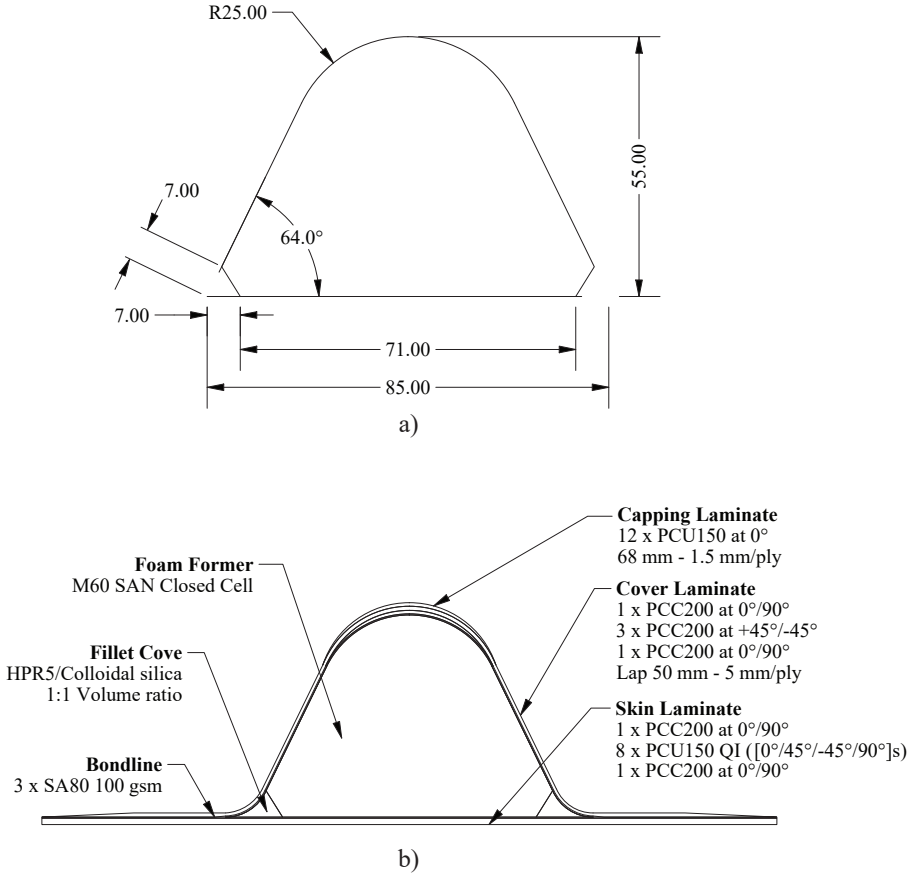

Figure 1. SSCP cross-sectional geometry and laminate details a) Stringer foam former cross-sectional dimensions, b) Laminate lay-up details. All dimensions are in millimetres [mm].

As seen in Fig. 2, the stringers were numbered as 1–3 based on their distance from the keel. *Stringer-1* was located closest to the keel edge, while *Stringer-3* was located closest to the chine edge. Similarly, the unsupported skin regions were numbered. *Skin-1* was located closer to the keel and *Skin-2* was located closer to the chine. The terms *keel-side* and *chine-side* were defined to designate which side

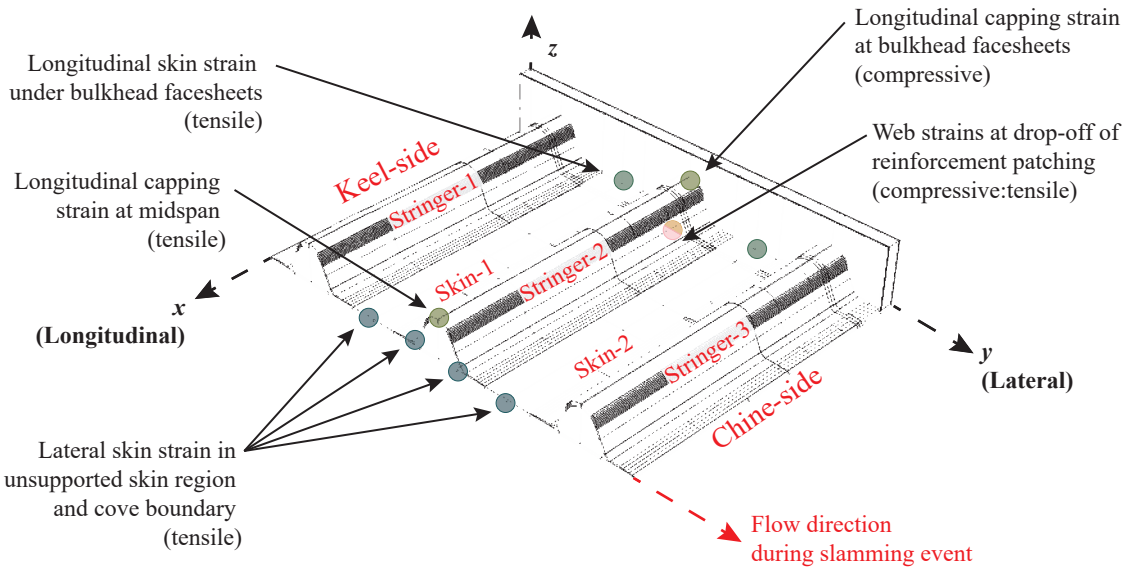

Figure 2. Schematic of SSCP slamming specimen. Due to symmetry along the longitudinal direction, only half of the specimen is displayed. The location of critical strains are indicated, along with the designation of the various skin and stringers

of the panel certain features were located. For example, the webs of the stringers were referred to as keel-side and chine-side. As the central stringer was fully bounded, it experienced the full passage of the pressure pulse from the Skin-1 (keel-side) midpoint to the Skin-2 midpoint (chine-side). As each stringer was expected to behave independently in a perpendicular impact orientation (Pearson et al., 2024), the free edges of Stringer-1 and Stringer-3 should not unduly influence the behaviour of Stringer-2. This meant that the response of the central stringer in the specimen should replicate the response of a stringer found on a much larger hull structure.

The flexible and rigid water impact of the slamming specimen was simulated at a constant velocity of 2.0 and 4.0 m s^{-1}, at an undeformed deadrise angle of 10°. While an entire craft will undergo global deceleration upon impact, from the perspective of a single hull panel, the impact is experienced with an approximately constant velocity (Battley et al., 2009). Therefore, constant velocity impact studies of hull panels more accurately represent real-world slamming events (Tveitnes et al., 2008). Strains at critical locations across the SSCP were compared between each test. These critical strains were identified during preliminary experimental testing, presented in Pearson et al. (2026c). The location and orientation of the strains is included within the naming convention:

$$\{\text{Designation}\}^{(\{\text{Distance from x-axis origin}\})}_{\{\text{Orientation}\}}$$

Three designations were defined: C for capping strains, S for skin strains, WK/WC for the keel- and chine-side web strains, and CK/CC for the keel- and chine-side skin strains at the cove boundary, and were numbered to refer to the stringer or skin region where the gauge is located. The x-axis origin was defined at the midspan of the specimen. The nomenclature for the critical strains considered in this work is outlined as follows:

- Stringer-2 [Central] longitudinal capping strains ($C2^{(0)}_{xx}$, $C2^{(490)}_{xx}$)
- Stringer-2 [Central] web strains ($WK2^{(290)}_{xz/zx}$, $WC2^{(290)}_{xz/zx}$),
- Monolithic longitudinal skin strains at the bulkhead facesheets ($S1^{(490)}_{xx}$, $S2^{(490)}_{xx}$)
- Monolithic lateral skin strains at the middle of unsupported regions ($S1^{(0)}_{yy}$, $S2^{(0)}_{yy}$)
- Monolithic lateral skin strains at the cove boundary of unsupported regions ($CK2^{(0)}_{yy}$, $CC2^{(0)}_{yy}$)

2.2 Numerical Setup

An examination of mechanisms of hydroelasticity requires the use of a two-way coupled model, where the structural response is able to influence the boundary conditions of the fluid. However, a two-way coupled analysis involves a significant computational cost, as each timestep must be iterated several times to achieve coupling convergence between disparate solvers (Causin et al., 2005). This is complicated by the need to adopt of under-relaxation methods to aid solution convergence (Causin et al., 2005), which result in further increases to associated the computational costs. In this work, a partitioned coupled approach was adopted, where separate fluid and structural solvers were run, with mesh deformation and pressure loading exchanged at each time step. The following sections outline the CFD, FEA, and coupling methodologies adopted for the hydroelastic analysis of SSCPs in water impacts.

2.2.1 CFD Methodology

The fluid model employed a simplified representation of the experimental SSTS setup, referred to as the *Simplified-domain* for the remainder of this paper. Compared to a similar model of the SSTS developed in Pearson et al. (2026b), computational costs were lowered through the use of a moving-fluid method (Pearson et al., 2026b), and a 80% reduction in the total volume of the domain by removing redundant regions located behind flow restriction plates. This reduced the overall the cell count from 6,490,648 to 1,234,020 cells. Additionally, the moving-fluid method used for the Simplified-domain is more suited for a two-way analysis as it removes additional mesh deformation caused by vertical translation of the panel, which simplifies data transfer between the solvers (Camilleri, 2017). However, the moving-fluid method limits the two-way coupled model to constant velocity impacts due to unrealistic levels of fluid inertia during non-constant velocity impacts. Due to a plane of symmetry along the midspan, only half of the fluid domain was modelled. Cells of 2.5 mm where defined along the wetted surface to capture the localised pressure pulse, which gradually increased in size away from the panel. Selection of the mesh was based on promising convergence behaviour for impact forces and pressures for a 10° deadrise impact, presented in Pearson et al. (2026b). This found that when using a 2.5 mm cell size, the numerical simulations had a relative error of less than 2%, with an uncertainty of less than 1% (Celik et al., 2008; Roache, 1994). Figure 3 presents an overview of the mesh and boundary conditions adopted in the Simplified-domain.

The air and water phases were solved as a compressible flow by the fluid solver. Such effects are usually only considered for flows approaching Mach 0.3 (Çengel et al., 2017), but the introduction of compressibility provides an additional level of damping to the coupling process, which greatly improves the stability of the solution (Camilleri, 2017; Yan et al., 2022). This proved to be essential, as solving the air and water phases as incompressible resulted in divergence of the coupled solvers. Air compressibility was solved using the ideal gas equation, and water compressibility was solved using the linear bulk modulus method in Equation 1 (Hayward, 1967):

$$\rho_w = \frac{\Delta P}{c_s^2}, \tag{1}$$

where:

ρ_w is the density of the water [kg m^{-3}]
ΔP is the difference from atmospheric pressure [Pa] (P_{atmos} =101,325 Pa)
c_s is the speed of sound through the fluid [m s^{-1}] (taken as 1,500 m s^{-1})

Camilleri (2017) investigated the effects of changes to the sonic speed in water impact models, and

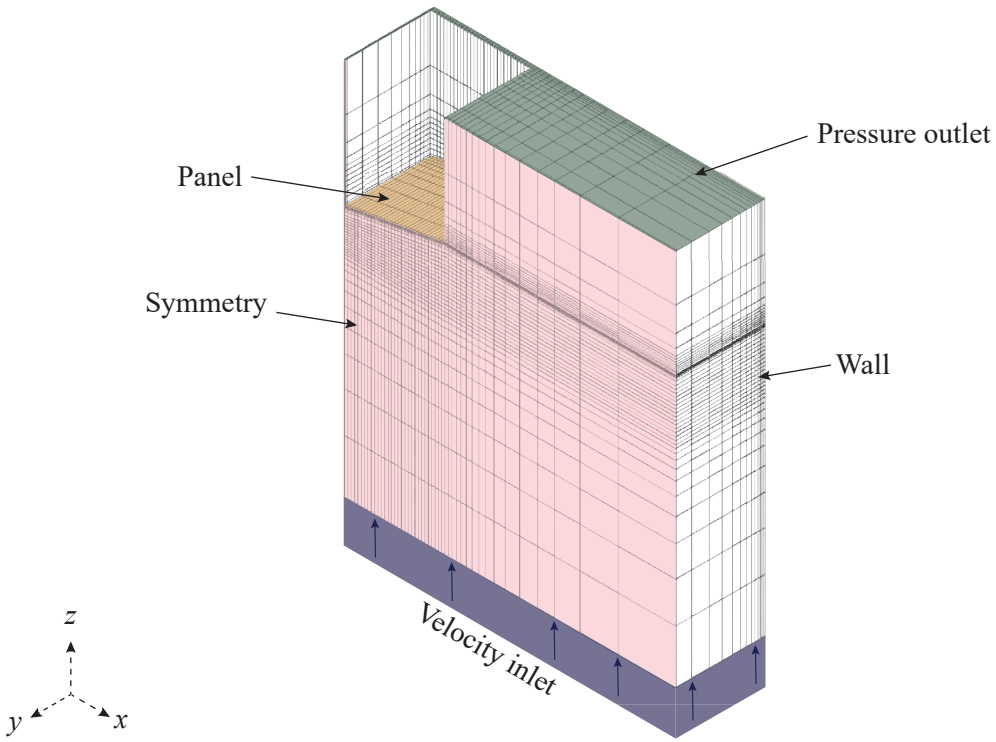

Figure 3. Boundary conditions of the Simplified-domain numerical slamming tank.

found that changes of up to 50% had a negligible effect on the solution. Use of a compressive fluid model in the Simplified-domain resulted in less than 1.0% change in slamming force and peak pressures for a rigid body impact compared to an incompressible fluid.

The fluid response was solved using Ansys Fluent 2022 R1. The implicit *Volume Of Fluid* (VOF) *Modified High-Resolution Interface Capturing* (MHRIC) scheme with interfacial anti-diffusion was selected (Ansys, Inc, 2017), as it was found to be accurate for use in water impact problems with highly structured meshes (Pearson et al., 2026b). Due to the promising balance between computational costs and convergence behaviour, Fluent's *Semi-Implicit Method for Pressure Linked Equations - Consistent* (SIMPLEC) pressure-velocity coupling method was selected (Ansys, Inc, 2017). The unsteady terms were discretised using a first-order implicit scheme, the convection terms were discretised using a second-order upwind scheme, and the pressure term was discretised using a *PREssure STaggering Option* (PRESTO) scheme.

2.2.2 FEA Methodology

The SSCP model was assembled using five independent parts: stringer, skin, foam former, bondline, and bulkhead. These parts were connected together using mesh tie constraints to form the full SSCP specimen (Bisagni et al., 2011; Vescovini et al., 2013; Vescovini and Bisagni, 2015). Each part was modelled as an individual entity to allow sudden changes in mesh densities at interfaces, such as between the bondline and the skin/stringer (Dassault Systemes, 2016). CFRP components in the skin and stringer were modelled using S4R conventional shell elements. The bondline between the stringer and skin was modelled using second-order C3D6 3D 6-node linear triangular prism elements and 0.3 mm thick COH3D8 8-node 3D continuum cohesive elements. The foam former and bulkhead parts were modelled with C3D8R linear brick, reduced integration elements. A global mesh size of 4.5 mm was selected, with 2.25 mm elements in the bond. This was based on promising convergence behaviour presented in Pearson (2025). This work indicated that when using a 4.5 mm global element size, the numerical simulations had a relative error of less than 2%, with an uncertainty of less than

5% (Celik et al., 2008; Roache, 1994). Additionally, the FEA methodology was found to accurately predict the stiffness response of an SSCP under a number of different out-of-plane loads cases.

An overview of the SSCP model used in this analysis is provided in Fig. 4. The bulkhead was fixed in placed along the top surface and pressure distributions were applied to the bottom surface of the skin. Materiel properties were obtained from coupon testing of PCU150 and PCC200 laminates (Pearson et al., 2026a). As in the fluid model, only half of the structural was modelled due to longitudinal symmetry planes. The final model was comprised of 101,604 elements and 119,215 nodes, and was solved using an implicit, non-linear Abaqus 2021 solver.

For one-way, non-hydroelastic impacts, a stiffness-proportional Rayleigh damping (Dassault Systemes, 2016) was included with a critical damping factor of 5% of the fully wetted natural frequency (31.2 Hz), which accounts for the 173.5 kg of water displaced by the impacting panel. This accounts for the additional energy dissipation and inertial effects resulting from the added mass of the displaced water in the structural response of the SSCP. This is significant, as the added mass of water is up to 40 times larger than the mass of the SSCP, and so dominates it's inertial response. Stiffness-proportional damping was employed as it limits the higher frequency behaviour that results from the rapid water impact loading (Dassault Systemes, 2016). A damped model displayed smooth water impact strain responses that were well validated against experimental measurements (Pearson, 2025). An equivalent undamped model featured spurious and nonphysical fluctuations in the predicted strain responses. When using a two-way coupling method, the added-mass from the displaced water is implicit, and its effect on the inertial response of the structure does not need to be specially accounted for within the FEA solver. The stiffness-proportional Rayleigh damping was reduced to a critical damping factor of 5% of the dry natural frequency (208.6 Hz). Similar levels of damping have been used in other studies investigating two-way coupling of water impacts (Camilleri, 2017; Xie et al., 2018).

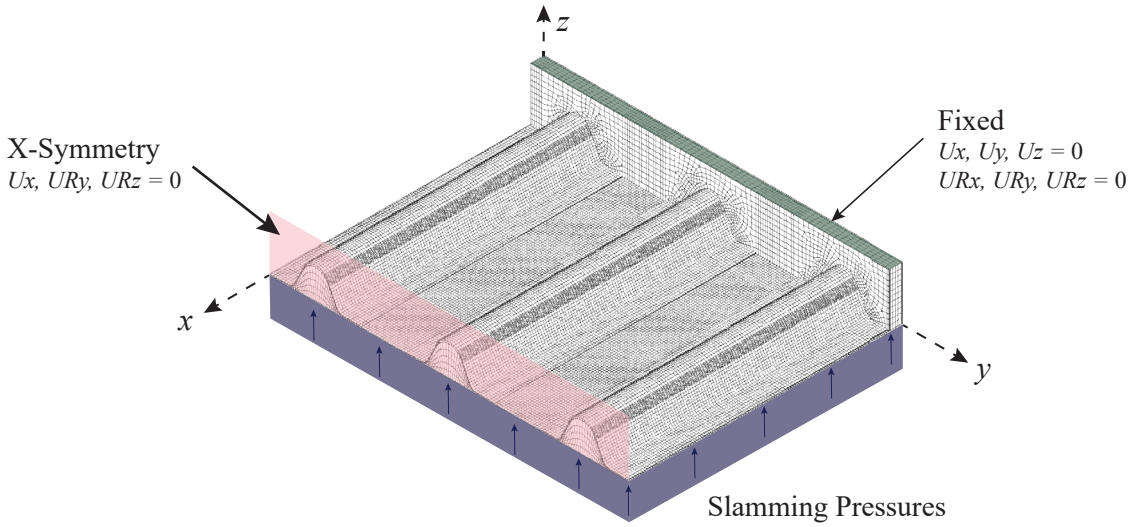

Figure 4. SSCP FEA setup for two-way coupling.

2.2.3 Coupling Methodology

Data transfer of the structural nodal displacements and fluid pressures was handled using the *MpCCI Coupling Environment* with a serial (Gauss-Seidel) algorithm (Fraunhofer SCAI, 2023). The structural and fluid solvers were solved in series, with data transfers occurring at the start and end of each iteration of the independent processes. This method maximises the efficiency of the available computational resources (Fraunhofer SCAI, 2023). Additionally, serial coupling methods exhibit more

promising convergence behaviour for strongly-coupled problems (Fraunhofer SCAI, 2023). The structural solver was selected to lead the coupling process, meaning it was the first to be calculated at each timestep, as this also exhibits more promising convergence behaviour (Fraunhofer SCAI, 2023). Figure 5 outlines the two-way coupling procedure used in this analysis. Each simulation was also repeated using a one-way coupled methodology, where the structural deformations were not passed back to the fluid solver. This ensures a rigid water impact, and allowed an investigation into the effects of hydroelasticity.

Pressure distributions and nodal deformations are transferred between the fluid and structural solvers by the MpCCI Coupling Environment using the *Shape Function* algorithm (Fraunhofer SCAI, 2023). Details of this algorithm are provided by Silva et al. (2009). The Quasi-Newton under-relaxation method with inverse Anderson mixing, a Jacobian parameter of 0.1, and one re-used level were selected as it promised to strongly accelerate and stabilise the convergence of mapped quantities (Koch, 2016). More information on Quasi-Newton relaxation methods is provided by Davis et al. (2022).

2.2.4 Simulation Parameters

A two-way coupled CFD-FEA analysis of the SSCP specimen was conducted for constant velocity impacts at 2.0 m s^{-1} and 4.0 m s^{-1}. Each impact was solved using 2000 timesteps, with a timestep size of 2.5e^{-5} s and 1.25e^{-5} s respectively. Selection of the timestep size was determined based on convergence behaviour presented in Pearson et al. (2026b). This gave a total solution time of 0.05 s and 0.025 s respectively. A maximum of 20 coupling iterations were allowed within each timestep (i.e. 20 data transfers between structural and fluid solvers), with a target residual of 1.0e^{-4}. Simulations were carried out using 16 cores and 128 GB of RAM on an AMD EPYC 7702P workstation, with a runtime of approximately 30 days each (720 hours).

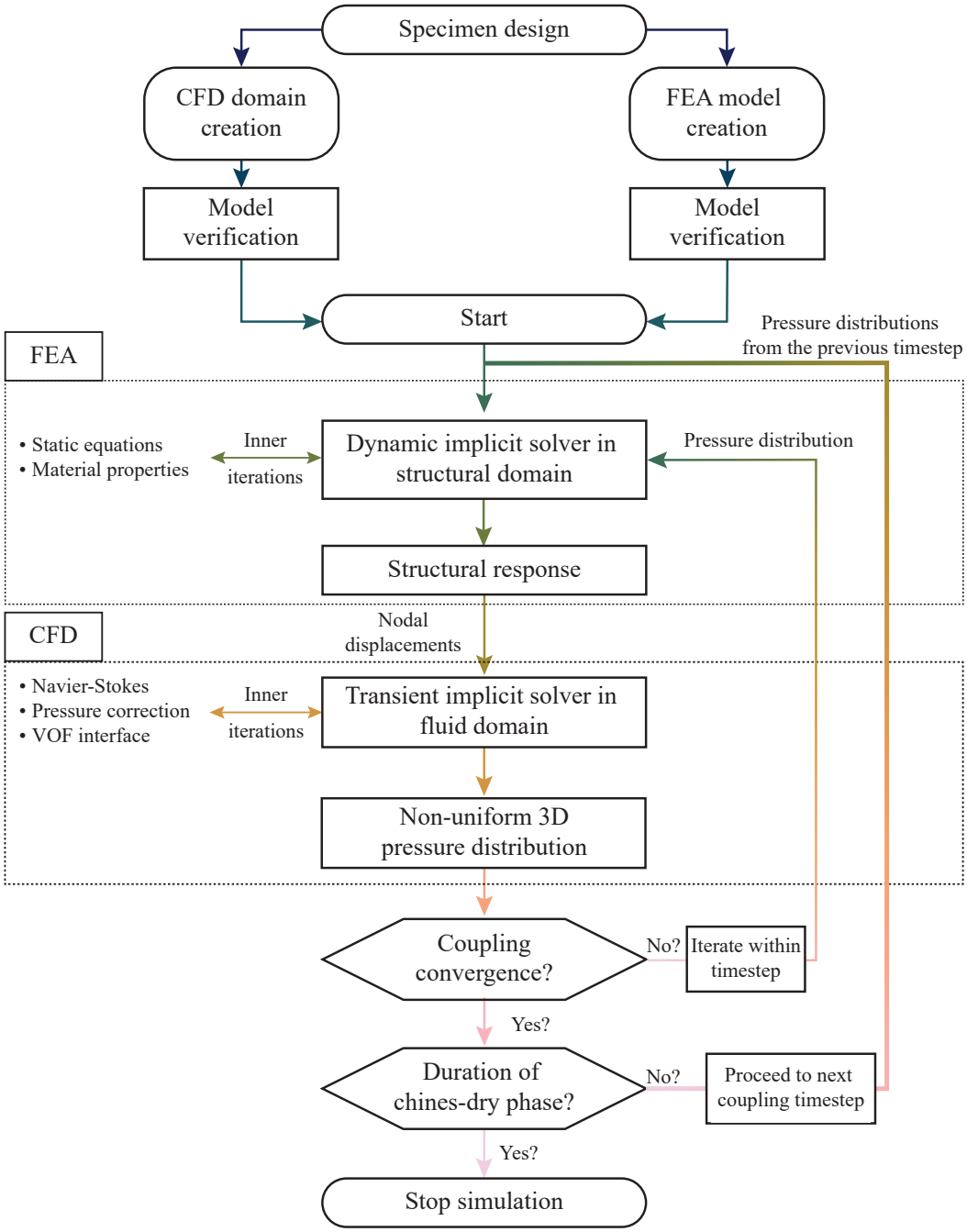

Figure 5. The partitioned, two-way, and strongly-coupled CFD-FEA procedure with a leading FEA solver for the water impact of an SSCP.

3 RESULTS

3.1 Influence of Hydroelasticity

In this work, the non-dimensional values of slamming and pressure coefficients are used. The advantage of this approach is that for a constant velocity rigid impact, plots of slamming and pressure coefficients are consistent for a given deadrise angle; they do not vary with impact velocity. Therefore, discrepancies between a plot of slamming and pressure coefficient for rigid and flexible impacts is related to the magnitude of the hydroelastic response. Slamming and pressure coefficients are calculated using Equation 2:

$$C_S = \frac{F}{0.5\rho V^2 BL}, \quad C_P = \frac{P}{0.5\rho V^2}, \tag{2}$$

where:

F is the vertical impact force [N]
P is the applied pressure [Pa]
ρ is fluid density [kg m^{-3}] (taken as 1,000 kg m^{-3})
V is the vertical impact velocity [m s^{-1}]
B is the wedge beam [m] (0.675 m)
L is the wedge span [m] (1.03 m)

3.1.1 Impact Forces

Figure 6 compares the slamming coefficient/immersion histories for rigid and flexible impacts. Slamming coefficients for 2.0 m s^{-1} were similar to the rigid impacts, but exhibit a slight undulating response, with relatively higher values located between 35–50 mm of vertical immersion. This is when the pressure pulse was located underneath the central stringer. During this period, the flexible 2.0 m s^{-1} impact slamming coefficient was comparable to the rigid impact. Peak slamming coefficient for the flexible 2.0 m s^{-1} impact was only 6.8% lower than the rigid impact. Flexible 4.0 m s^{-1} impacts displayed up to 25% lower slamming coefficients than the rigid impact at all immersion lengths. This indicates that hydroelastic effects result in a less severe and dynamic impact event, which agrees with the experimental measurements in Pearson et al. (2026c).

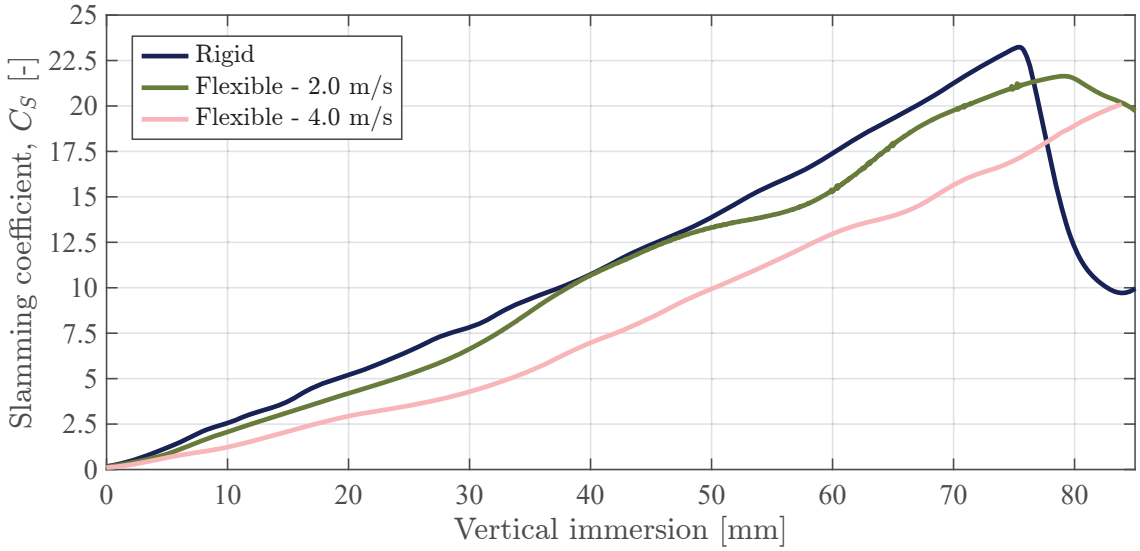

Figure 6. One- and two-way coupling slamming forces for the Simplified-domain.

3.1.2 Impact Pressures

Pressure Distributions. The pressure distributions along the panel's wetted surface halfway through a rigid and flexible impact (immersion depth of 50 mm) are presented in Fig. 7. Dashed lines are included in the figure to indicate the location of the stringers, as these regions represent a large change in local stiffness, and likely influences the hydroelastic behaviour.

Throughout the chines-dry phase, rigid impacts (Fig. 7a) featured a convex pressure pulse shape (due to separation gaps between the lateral edges of specimen (Pearson et al., 2026b)). However with the introduction of hydroelasticity in flexible impacts, the pressure pulse became distorted and smeared along the span of the panel, which became more pronounced at higher impact velocities. At

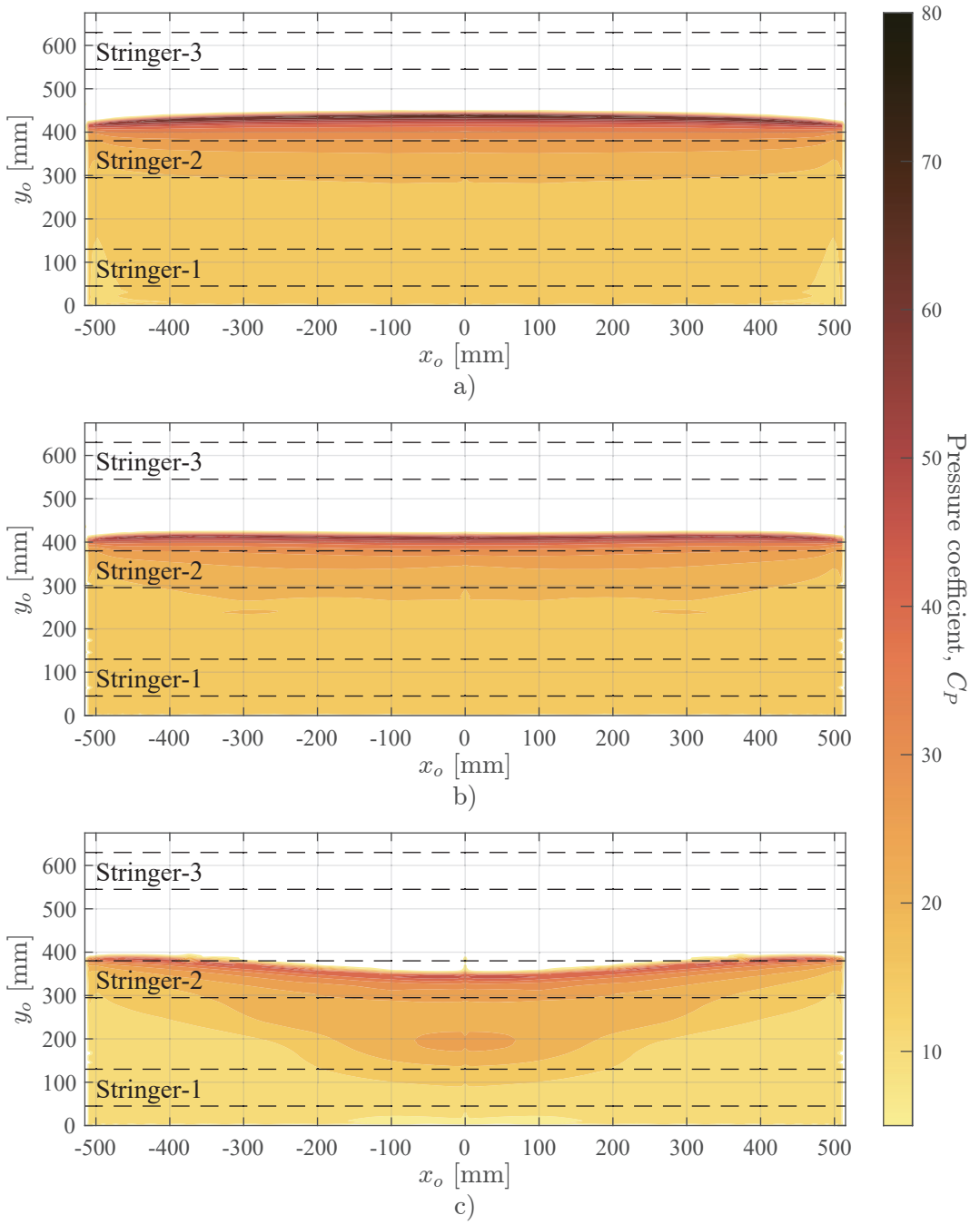

Figure 7. Water impact pressure distributions for rigid and flexible stiffened panels. a) Rigid, b) 2.0 m s^{-1} flexible, and c) 4.0 m s^{-1} flexible.

2.0 m s^{-1} (Fig. 7b), the pressure pulse had lost its curvature and becomes flat/straight along the span of the specimen. At 4.0 m s^{-1} (Fig. 7c), the pressure pulse had become concave and the distribution at the midspan lagged behind by the edges by up to 40 mm. At 50 mm of vertical immersion, a rigid impact predicted the pressure pulse at the midspan to lead the lateral edges by 3.4% of the panel's beam. For a 2.0 m s^{-1} flexible impact, this was reduced to 0.9%. For a 4.0 m s^{-1} flexible impact, the pressure pulse at the midspan lagged behind the lateral edges by 5.1% of the panel's beam. This indicates that hydroelasticity results in a reduction in the propagation velocity of the pressure pulse at the midspan; it takes more time for the flow-front to travel from the panel's keel to chine. However, hydroelastic effects are less significant away from the midspan due to decreased deformations of the panel. A higher velocity of the flow-front away from the midspan produces a concave pressure distribution.

Pressures and Kinematics. Impact pressures are a function of deadrise angle and impact velocity, and so the relationship between the kinematic changes and the arrival of the pressure pulse must be considered. Deflections, relative impact velocities, local deadrise angles, and pressures were analysed for five locations along the midspan of the specimen. These were located under Stringers-1–2 (C1 and C2), and the keel-side, centre, and chine-side of the skin region (K-S1, S1, and C-S1 respectively). The relative locations of these analysis points are displayed in Fig. 8. Figure 9 displays the kinematics of the analysis points defined in Fig. 8 for a 4.0 m s^{-1} flexible impact. Normalised pressure/immersion histories in Fig. 9a determine where the pressure pulse was located, and if there is a relationship between kinematic behaviour and localised loading. The pressure histories for the same points during a rigid impact are included as dashed lines, which indicates flexible pressure/immersion histories are reduced and delayed compared to rigid impacts.

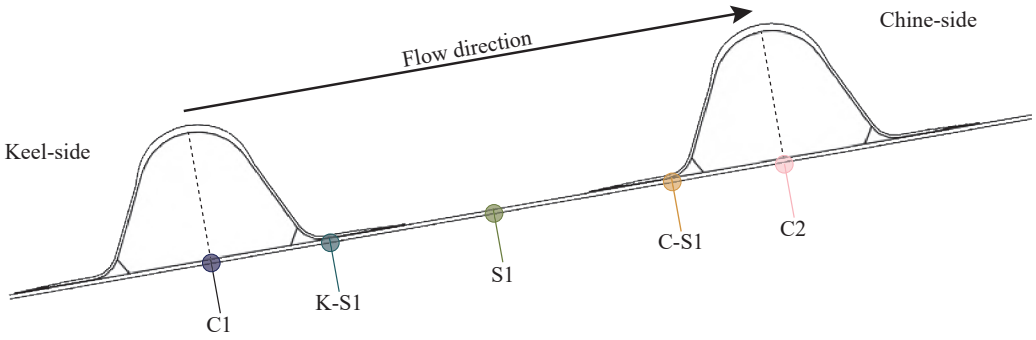

Figure 8. Kinematic analysis points in first skin region.

The kinematic behaviour of the SSCP was sequential, with locations closer to the keel (C1 and K-S1) deforming earlier into the impact event than regions located closer to the chine. Deflections lead to changes in the relative velocities between the skin and the water, leading to a reduction in the effective local impact velocity (i.e. at S1 down to 0.12 m s^{-1}, Fig. 9c). Increased deflections of the skin also led to curvature and changes in the local deadrise angle. On the keel-side, the skin region experienced an increase in the local deadrise angle (K-S1) up to 15°, while the at the centre, there was a decrease in the local deadrise angle (S1) to 3.3°.

After the pressure pulse passed S1, the chine-side skin region began to be loaded and deflect. The relative impact velocity and local deadrise angle at C-S1 were reduced to 0.41 m s^{-1} and 3.3° respectively. However when the pressure pulse arrived at C-S1 after 46.4 mm of vertical immersion, the rate of C-S1 deflections began to slow, leading to an increase in relative impact velocities to 1.2 m s^{-1}. A higher impact velocity (compared to S1) and a reduction in local deadrise angle results in a 100% and 30% higher pressure peaks at C-S1 compared to K-S1 and S1 respectively. This increase in peak pressure propagated an increased residual pressure back to S1, resulting in a secondary peak at 46.4 mm of vertical immersion. This was 15.7% later into the chines-dry phase than a rigid impact would predict (i.e. at the arrival of the pressure pulse). Importantly, this indicates that the maximum pressures experienced by the unsupported skin are delayed due to hydroelastic behaviour at the chine-side edge, and are lower than a rigid impact would predict (Fig. 9a).

The effects of kinematic changes (relative velocities and local deadrise angle) between a rigid and flexible impact at 40 mm vertical immersion are displayed in Fig. 10 and Fig. 11. Changes in local deadrise were negligible under the stringer, but may experience a 40–60% change in the skin region. This resulted in an increase in local deadrise at the keel-side edge of the unsupported skin region (K-S1) and a decrease at the chine-side edge (C-S1), thereby influencing the local pressures. In this case, the skin and stringers deform more than 3.5–6.0 mm at the panel's midspan (i.e. a skin deflection of 0.61% of the panel's span, 2.4% of the stringer's spacing and 360% of the skin's thickness). This indicates that hydroelastic effects become significant with relatively small out-of-plane deflections, which are likely to occur during operation of a high-performance racing yacht.

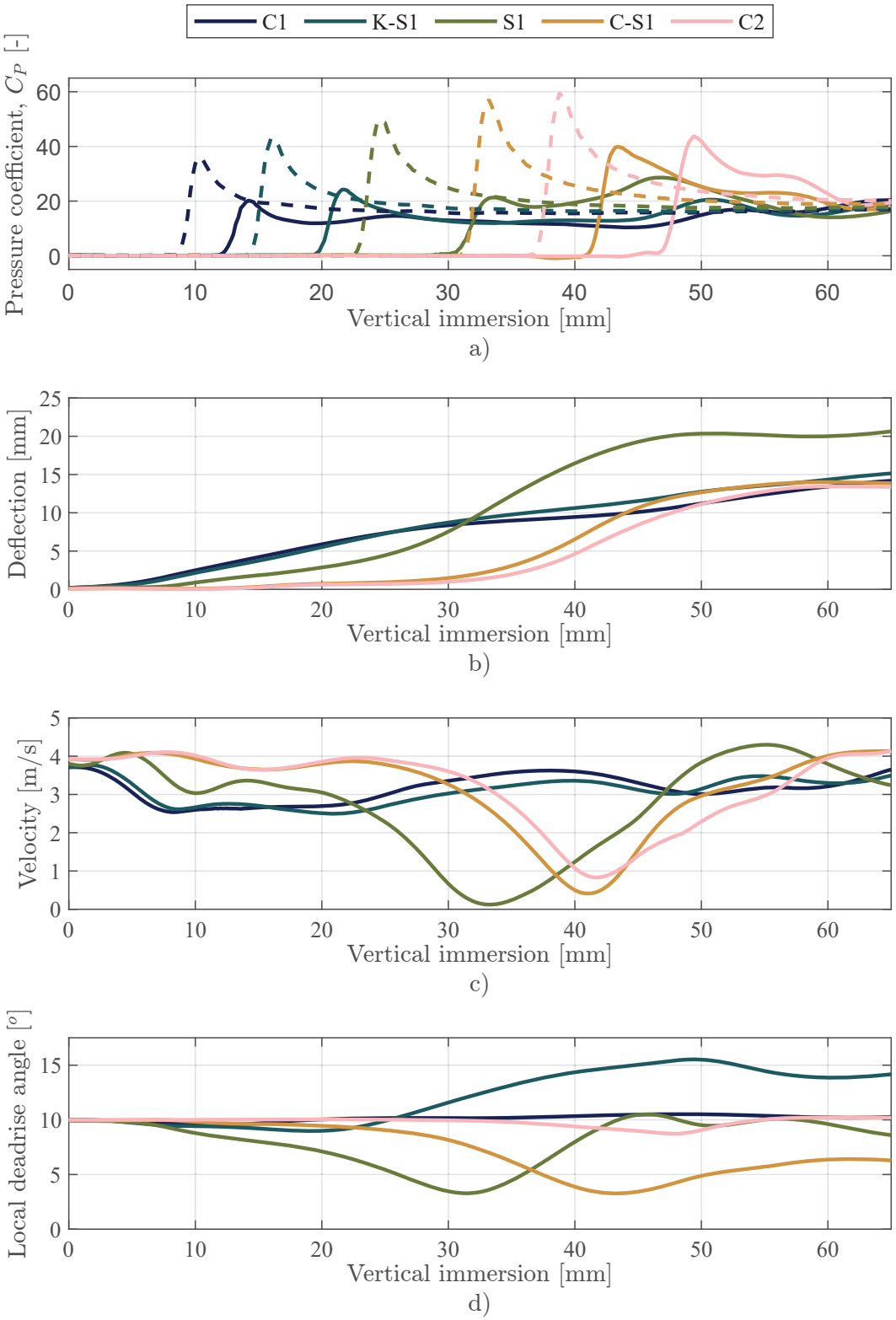

Figure 9. Pressures and kinematics of skin region for a 4.0 m s^{-1} flexible water impact. a) Pressures (rigid results are presented as dashed lines), b) Deflections, c) Relative impact velocities, and d) local deadrise angle.

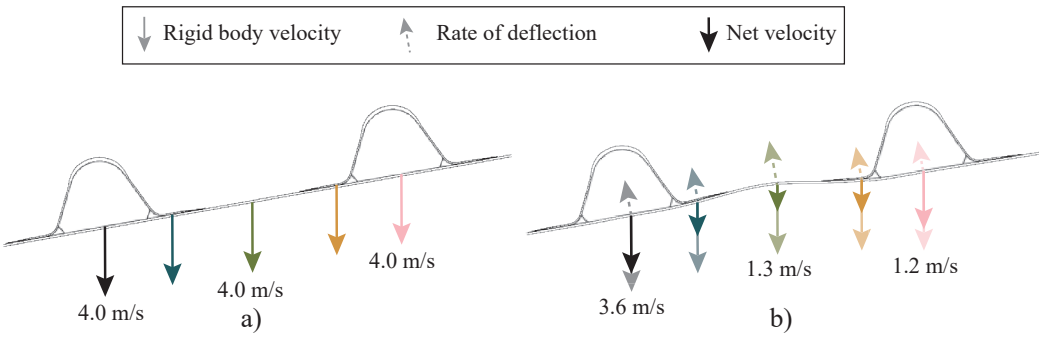

Figure 10. Relative impact velocities of the SSCP specimen at 40 mm immersion for a) Rigid and b) Flexible 4.0 m s^{-1} water impacts.

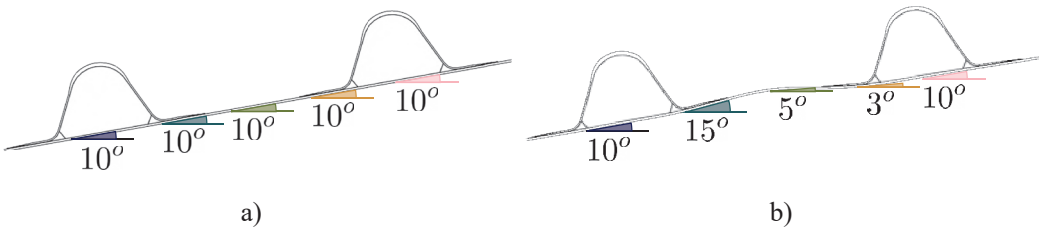

Figure 11. Changes in local deadrise angle of the SSCP specimen at 40 mm immersion for a) Rigid and b) Flexible 4.0 m s^{-1} water impacts.

3.1.3 Strain Responses During a Water Impact

Figures 12–13 present a comparison of the critical strains (lateral skin, stringer capping, and web strains) for rigid and flexible impacts at 2.0 m s^{-1} and 4.0 m s^{-1} respectively. Lines A(R), B(R), and C(R) indicate when the pressure pulse at the midspan had reached the centre of Skin-1, Stringer-2, and Skin-2 (Fig. 2) of the SSCP specimen during a rigid water impact. Lines A(F), B(F), and C(F) indicate when the pressure pulse at the midspan had reached the centre of Skin-1, Stringer-2, and Skin-2 of the SSCP specimen during a flexible water impact. As the pressure pulse propagation velocity is reduced for flexible water impacts, lines A(F), B(F), and C(F) lag behind A(R), B(R), and C(R).

Lateral Skin Strains. The lateral skin strains in for flexible water impacts ($S1^{(0)}_{yy}$(F) and $S2^{(0)}_{yy}$(F)) feature a broader peak in Fig. 12 and Fig. 13 compared to the rigid impacts ($S1^{(0)}_{yy}$(R) and $S2^{(0)}_{yy}$(R)) as distortion and slow down of the pressure pulse results in a longer loading period. Despite this, peak strains were still reported just after the passing of the pressure pulse under these locations (A(F) and C(F) respectively). This indicates that hydroelastic effects do not modify the relative timing of the skin strain responses during an impact; peak lateral skin strains occur as the pressure pulse passes underneath the unsupported skin region.

At 2.0 m s^{-1} (Fig. 12), the peak strains for rigid and flexible impacts were similar. Peak strains in a flexible impact were up to 5.8% less than a rigid impact and occurred 7.3–8.7% later into the chines-dry phase for $S1^{(0)}_{yy}$, indicating hydroelastic effects were minimal. At 4.0 m s^{-1} (Fig. 13), flexible impact peak strains were 6% lower than rigid impacts and occurred 16.5% later into the chines-dry phase. This indicates a stronger hydroelastic response with increases in impact velocity.

Longitudinal Capping Strains. Longitudinal capping strains in Fig. 12 and Fig. 13 exhibit a rapid increase from A–B, followed by an inflection point around B, and a more gradual increase in strains from B–C. This is due to the change in the rate of load application as the pressure peak propagates

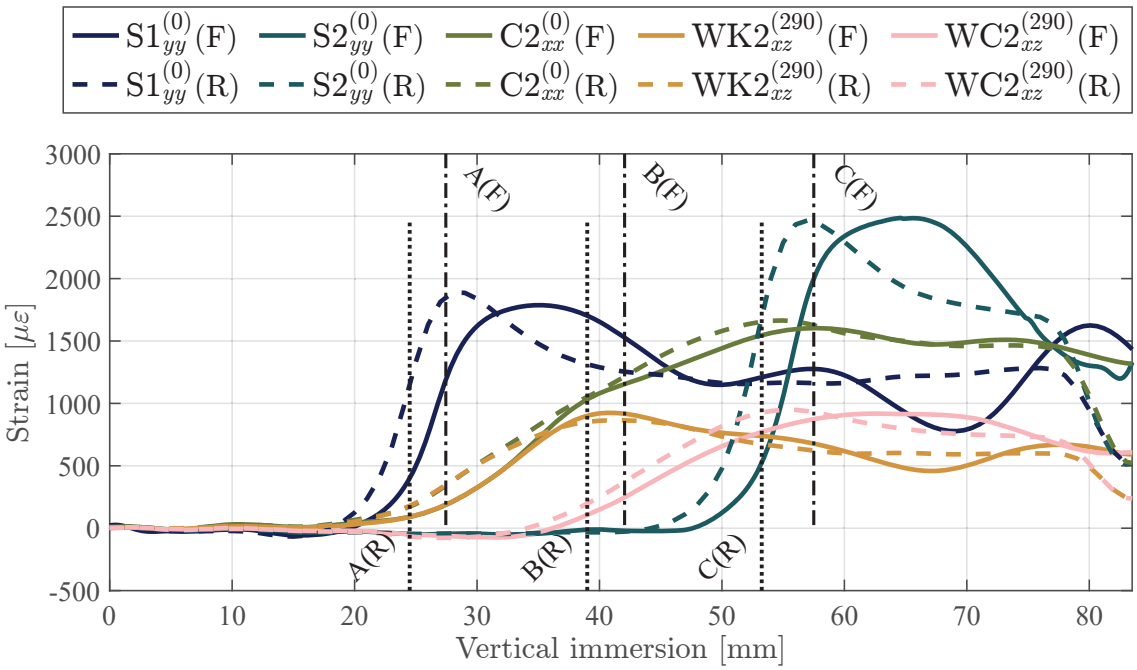

Figure 12. Rigid and flexible strain responses of the SSCP during a 2.0 m s^{-1} water impact.

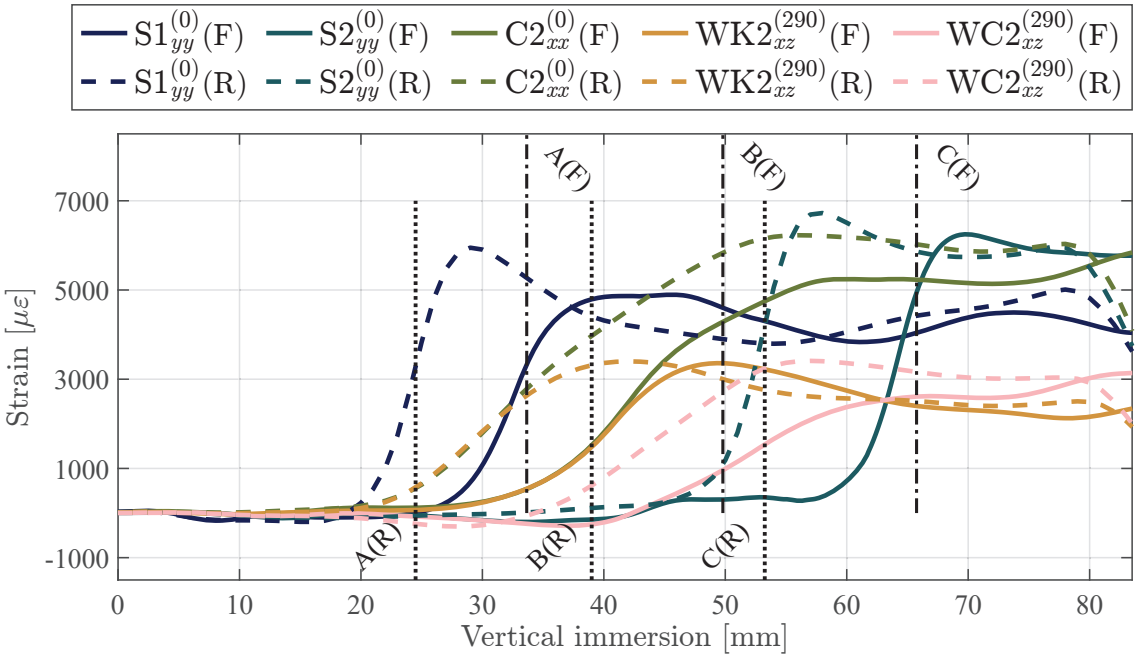

Figure 13. Rigid and flexible strain responses of the SSCP during a 4.0 m s^{-1} water impact.

underneath the stringer (Pearson, 2025). As seen in the lateral skin response, strains for a 2.0 m s^{-1} flexible impact (Fig. 12) were closely aligned in timing and magnitude with its rigid counterpart. A 4.0 m s^{-1} flexible impact (Fig. 13) had a 16% reduction in the peak strain response which occurred 6% later into the chines-dry phase. This confirms that hydroelasticity reduces the magnitude of peak strains, even for structures that are more affected by global load, and becomes more significant with increases in impact velocity.

Web shear strains. For rigid and flexible impacts, peak keel-side web strains occurred as the pressure pulse at the midspan passed underneath the central stringer (B(R) and B(F)). Peak chine-side strains occurred as the pressure pulse crossed the middle of the adjacent unsupported skin region (C(R) and C(F)). Flexible web strains reported a higher peak strains for the keel-side ($WK2^{(290)}_{xz}$(F))

compared to the chine-side (WC2$_{xz}^{(290)}$(F)) which agrees with the observations from experiments (Pearson et al., 2026c). This is in contrast to the rigid impact results, which predicted higher strains in the chine-side web compared to the keel-side web. At 4.0 m s^{-1} (Fig. 13), despite a 36% reduction in total panel load and lower peak pressures during a flexible impact, WK2$_{xz}^{(290)}$(F) was only 5% lower than WK2$_{xz}^{(290)}$(R). In contrast, WC2$_{xz}^{(290)}$(F) was 22% lower than WC2$_{xz}^{(290)}$(R).

This behaviour can be explained in terms of hydroelasticity of the panel. Increases in relative impact velocity, pulse propagation velocity, and a decrease in deadrise angle underneath the keel-side web results in an increase in pressure peak. This occurs as the pressure pulse passes underneath a stringers keel-side web (from A(F)–B(F)). The opposite occurs as the pressure peak passes underneath the stringers chine-side web (From B(F)–C(F)), where there are decreases in relative impact velocity, pulse propagation velocity, and an increase in deadrise angle. This means that the stringers keel-side web carries more shear load compared to the chine-side web, resulting in higher keel-side web strains and reduced chine-side web strains. This indicates that the keel-side web is more critical to the SSCP than the chine-side web.

Additional Strain Responses. Figures 14–15 present the additional critical strain responses. These include longitudinal skin and capping strains underneath the bulkhead facesheets (S1$_{xx}^{(490)}$, S2$_{xx}^{(490)}$, and C2$_{xx}^{(490)}$) and cove-former boundary strains on either side of the central stringer (keel-side CK2$_{yy}^{(0)}$ and chine-side CC2$_{yy}^{(0)}$). Capping strains at the bulkhead were compressive, and so the absolute values of C2$_{xx}^{(490)}$ are presented here.

For a 2.0 m s^{-1} rigid impact (Fig. 14), CK2$_{yy}^{(0)}$(R) and CC2$_{yy}^{(0)}$(R) were 2.4% and 21.5% less than their unsupported skin strains (S1$_{yy}^{(0)}$(R) and S2$_{yy}^{(0)}$(R)). For a 2.0 m s^{-1} flexible impact, CK2$_{yy}^{(0)}$(F) was 5% higher than S1$_{yy}^{(0)}$(F), while the CC2$_{yy}^{(0)}$(F) was 10% lower than S2$_{yy}^{(0)}$(F). Note that CK2$_{yy}^{(0)}$(F) and CC2$_{yy}^{(0)}$(F) were 1.8% and 14.6% higher than CK2$_{yy}^{(0)}$(R) and CC2$_{yy}^{(0)}$(R) respectively for a 2.0 m s^{-1} impact. This is the first indication that the strain response during a flexible impact results in higher peak strains compared to a rigid impact, confirming the critical nature of the cove-former boundary, where failures are likely to occur (Pearson et al., 2026c).

At 4.0 m s^{-1} (Fig. 15), CK2$_{yy}^{(0)}$(F) and CC2$_{yy}^{(0)}$(F) were up to 14.5% and 17% higher than S1$_{yy}^{(0)}$(F) and S2$_{yy}^{(0)}$(F), and were the highest strains predicted during a water impact. Comparison of the results in Fig. 12–15 indicates that the highest predicted strains in the SSCP in a 4.0 m s^{-1} flexible impact occurred in the outermost skin ply along the cove-former boundary. This indicates that the cove-former boundary strains become the critical response as impact velocities increase through a combination of increased membrane mechanisms in the unsupported skin (due to larger skin deflections) and stress concentrations along the edge of the cove. This agrees with the conclusions of Pearson et al. (2026c) and with the tensile fractures along the cove-former boundary of the experimental specimen. Unlike the 2.0 m s^{-1} impact, flexible impact predictions at 4.0 m s^{-1} for CK2$_{yy}^{(0)}$(F) and CC2$_{yy}^{(0)}$(F) were 17.2% and 3.2% less than CK2$_{yy}^{(0)}$(R) and CC2$_{yy}^{(0)}$(R) respectively, but this is likely a function of the reduced pressures and forces applied to the structure due to hydroelasticity, which results in less deflection and membrane mechanisms in the skin.

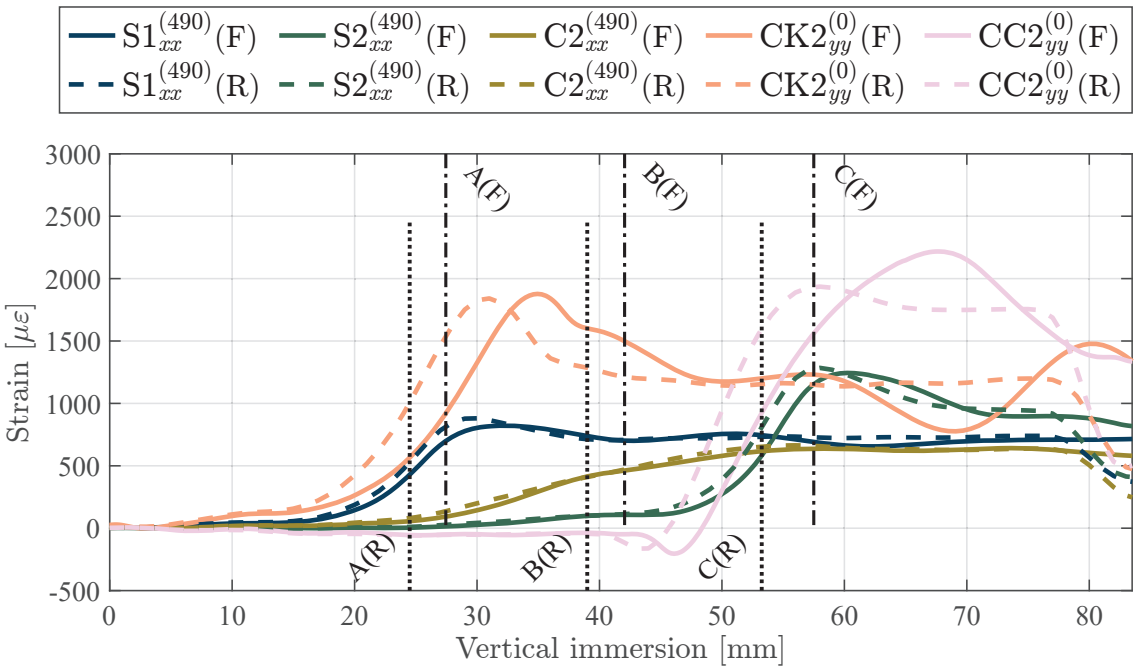

Figure 14. Additional rigid and flexible strain responses of the SSCP during a 2.0 m s^{-1} water impact.

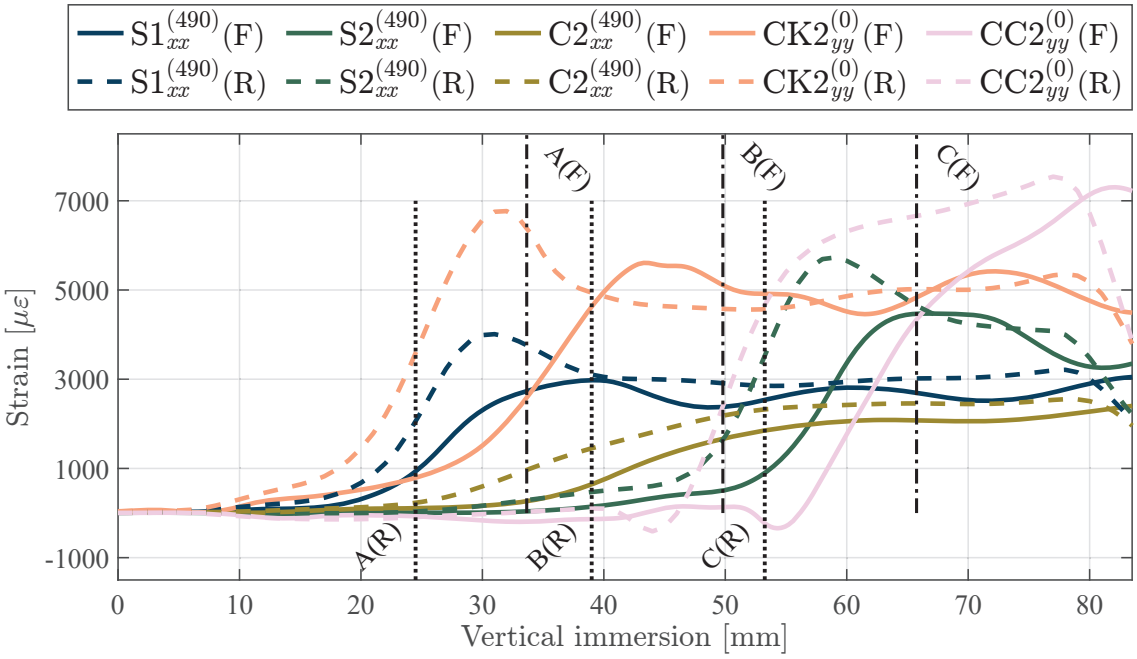

Figure 15. Additional rigid and flexible strain responses of the SSCP during a 4.0 m s^{-1} water impact.

3.2 Comparisons of Uniform Pressures, Rigid Impacts, and Flexible Impacts

A range of static out-of-plane uniform pressures were applied to the slamming specimen model. No other changes were made to the FEA setup. This ensures the same model and boundary conditions have been analysed in static uniform pressures, rigid one-way water impacts, and flexible two-way water impacts. Figure 16 presents the predicted strain response for critical skin, capping, and web strains as a function of an applied uniform pressure. Peak strains for a 4.0 m s^{-1} constant velocity water impact are included in the figure to compare the equivalent uniform pressures required to produce the same strains as a quasi-static rigid (R-S), dynamic rigid (R-D) and a dynamic flexible impact (F). By comparing predictions from all three methodologies, it is possible to quantify the discrepancies with simplifications to the load case. Note that the dynamic flexible impact strains are taken here to

represent the 'true' slamming response of the SSCP. Due to specimen and load symmetry for the uniform pressure load, several of the strain locations report an identical strain response (and so their plots overlap in Fig. 16), such as:

- Longitudinal skin strains $S1_{xx}^{(490)} == S2_{xx}^{(490)}$
- Lateral skin strains $S1_{yy}^{(0)} == S2_{yy}^{(0)}$
- Cove-former boundary strains $CK2_{yy}^{(0)} == CC2_{yy}^{(0)}$
- Stringer web strains $WK2_{xz}^{(290)} == WC2_{xz}^{(290)}$

Figure 16 indicates that no single uniform pressure load is able reproduce the peak strain state of a slamming SSCP. The capping strain ($C2_{xx}^{(0)}$) for a flexible water impact corresponds to a 163 kPa uniform pressure load. However, the peak lateral skin ($S2_{yy}^{(0)}$) and web strains ($WK2_{xz}^{(290)}$) recorded during the same impact correspond to an equivalent uniform pressure of 229 kPa and 200 kPa respectively. A uniform pressure that produces the same strain state in the capping laminate underpredicts the strains in the skin and web by 14% and 54% respectively for the same water impact. This is due to the difference in sensitivity of the skin and stringer to the local and global out-of-plane loads. For regions more influenced by local loads (such as the skin), a uniform pressure that produces the same global load will underpredict the strain response of the skin, which may lead to premature failure of the skin during operation. Conversely, for regions more influenced by global loads (such as the stringer), a uniform pressure that produces the same skin strains will overpredict stringer strains and lead to redundant weight in the structure.

Results in Fig. 16 indicate that rigid impacts result in an overprediction of peak strains compared to a flexible impact, which agrees with the findings of Section 3.1.3. The largest discrepancies occurred for longitudinal skin strains underneath the bulkhead facesheets ($S2_{xx}^{(490)}$), with an overprediction of 31.3% and 33.6% for the dynamic and quasi-static predictions respectively. The quasi-static rigid impact results in up to a 3.9% larger overprediction than the dynamic rigid impact for every critical strain response. This is still less than the largest overprediction that results from an equivalent uniform pressure (65.8% for $S1_{xx}^{(490)}$) This indicates that despite the overpredictions of a rigid impact model, it provides a better representation of the true flexible slamming SSCP strain state than any single equivalent uniform pressure. Improvements to structural efficiency and resiliency may be possible if a rigid impact analysis is incorporated into the design process. Importantly, the results from a rigid impact prediction were conservative across all compared metrics under the studied conditions, which implies that it results in in-built safety factors and redundancy to the final design.

The Authors note that design standards already call for different design pressures for the skin and stringers (ISO, 2019); the skin could be designed to a higher uniform pressure than the stringer. However, these pressures as a design load are poorly justified, and the standard methodology assumes each component to act in isolation, and not part of a full panel (i.e., the skin acts as a fully fixed plate, while the stringer acts as a isolated beam). Such assumptions might not be valid for the efficient and resilient design of a high-performance racing yacht, and a future investigation into this problem is required.

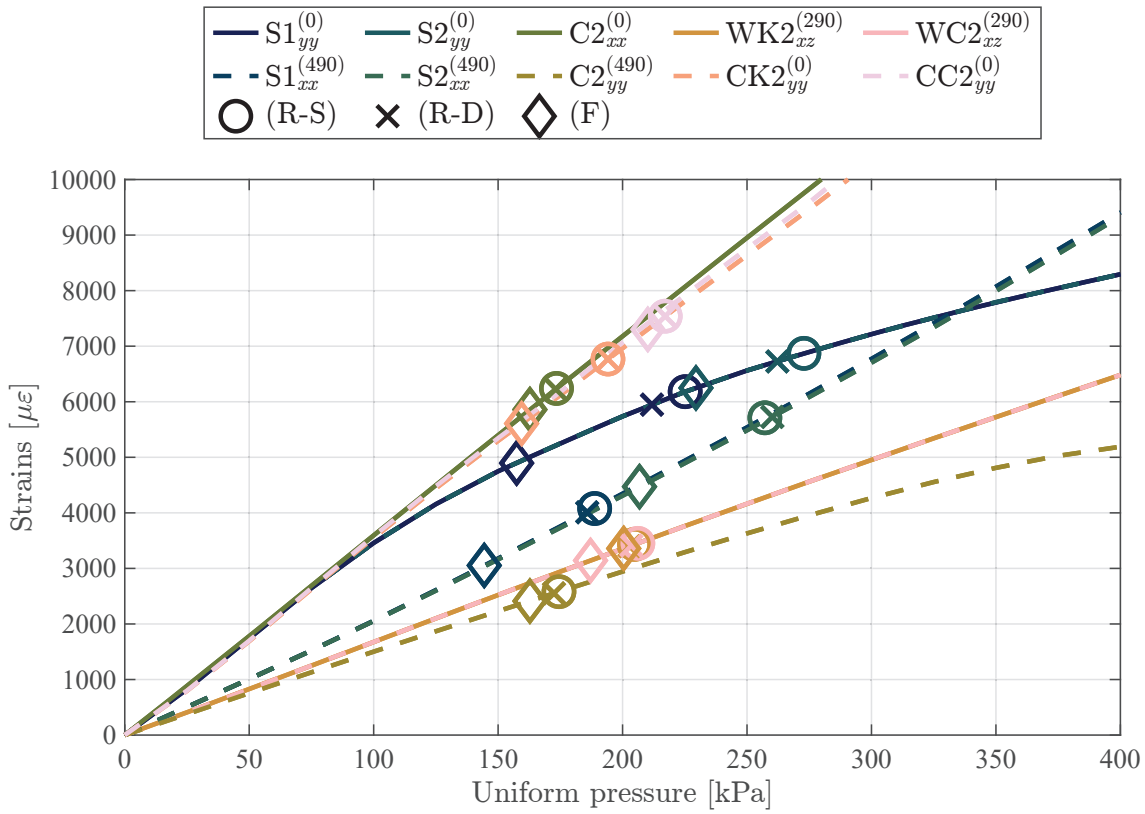

Figure 16. Strains at critical locations as a function of applied uniform pressure load. Peak slamming strains for a 4.0 m s^{-1} rigid and flexible impact (denoted by the shape of the symbol) at the same locations (denoted by the colour of the symbol) are indicated on the figure. Note due to specimen and load symmetry for a uniform pressure, several critical strains report an identical strain response, resulting in an overlap of the plotted lines.

4 SUGGESTIONS TO IMPROVE THE DESIGN LOAD CASE

The challenge is synthesising a methodology that incorporates the non-uniform pressure distribution and can feasibly be used during the design process. However, results presented in Pearson et al. (2024), Pearson et al. (2026c), Pearson et al. (2026a), and Sections 3.1.3 and 3.2 indicate that:

1. Hydroelasticity decreases the severity of a slamming event under the studied conditions. The omission of hydroelastic behaviour may result in a naturally conservative design.
2. Inertial effects within the structure are often minimal due to the large pressures and the thin/light construction of high-performance SSCPs. A rigid impact may reasonably be approximated as a quasi-static event, with only a 33.6% overprediction compared to the 65.8% from a uniform pressure.
3. The application of a non-uniform pressure distribution is more accurate than any single uniform pressure.
4. Regardless of the impact velocity of a rigid impact, the relative timings (during immersion) of peak strains in the skin and stringer are only dependant on the location of the pressure pulse along the wetted surface.
5. Laminate failures of SSCPs can be reasonably predicted using the Maximum Strain failure criteria, with data obtained from uniaxial coupon testing.

The lack of significant inertial behaviour and predictable timing of peak strains indicates that the critical strains in the skin, capping, and web of a slamming SSCP can be determined by statically solving for a series of key instants, rather than the entire slamming event. This reduces the computational costs associated with simulating a slamming SSCP. The location and shape of a quasi-two-dimensional pressure distribution for a given deadrise and impact velocity can be obtained without costly fluid simulations from an analytical asymptotic solution (Zhao and Faltinsen, 1993). The equations developed by Zhao and Faltinsen (1993) are presented in Equations 3–4.

$$\text{for } 0 \leq x \leq c(t),\ P(x) = \frac{\rho V c\left(\frac{\mathrm{d}c}{\mathrm{d}t}\right)}{\sqrt{c^2 - x^2}} - \frac{\rho V c\left(\frac{\mathrm{d}c}{\mathrm{d}t}\right)}{\sqrt{2c(c-x)}} + \frac{2\rho\left(\frac{\mathrm{d}c}{\mathrm{d}t}\right)^2 \sqrt{|\tau|}}{(1+\sqrt{|\tau|})^2}, \tag{3}$$

$$\text{for } x \geq c(t),\ P(x) = \frac{2\rho\left(\frac{\mathrm{d}c}{\mathrm{d}t}\right)^2 \sqrt{|\tau|}}{(1+\sqrt{|\tau|})^2}, \tag{4}$$

where:

- P is the pressure along the x-axis [Pa]
- x is the horizontal distance from the keel [m]
- ρ is the fluid density [kg m^{-3}]
- β_r is the deadrise angle measured in radians [rad]
- c is the location of the contact point along x ($0.5\pi x$) [m]
- V is the instantaneous vertical velocity [m s^{-1}]
- τ is a parameter that is numerically determined based on the jet thickness δ using:

$$x - c = \frac{\delta}{\pi}\left(ln|\tau| - 4\sqrt{|\tau|} - |\tau| + 5\right), \quad \text{where } \delta = \frac{2\pi x V^2}{\left[4\left(\frac{\mathrm{d}c}{\mathrm{d}t}\right)\right]^2} \tag{5}$$

Figure 17 presents the critical strain responses of the slamming specimen during a perpendicular orientation, 2.0 m s^{-1} constant velocity quasi-static rigid impact, with pressure distributions derived from the analytical asymptotic solution (Zhao and Faltinsen, 1993). The panel was treated as fully bounded (as would occur inside a hull structure), and so the highest capping strains were compressive and occur under the bulkhead facesheets. Results are presented as a function of the pressure pulse location along the wetted surface of the SSCP, as illustrated in Fig. 18. At 0 mm, the pulse was located underneath the middle of the keel-side unsupported skin region. At 125 mm, the pressure pulse was located underneath the stringer, and at 250 mm, it was located underneath the middle of the chine-side unsupported skin region.

Due to the use of a static solver and omission of hydroelastic behaviour, the relative timing of peak strains is solely a function of the pressure pulse location and SSCP configuration. Changes to impact velocity do not influence the relative timing of peak strains, only their magnitude. The unsupported skin ($S1^{(0)}_{yy}$ and $S2^{(0)}_{yy}$) reported peak strains just after the passing of the pressure pulse, when it was located at 15 mm and 265 mm respectively. Peak keel-side strains ($WK2^{(290)}_{xz}$) occurred as the pressure pulse crossed underneath the stringer (125 mm). Peak chine-side and capping strains occurred as the pressure pulse crosses the middle of the chine-side unsupported skin region (245–275 mm), and is when the stringer was most loaded.

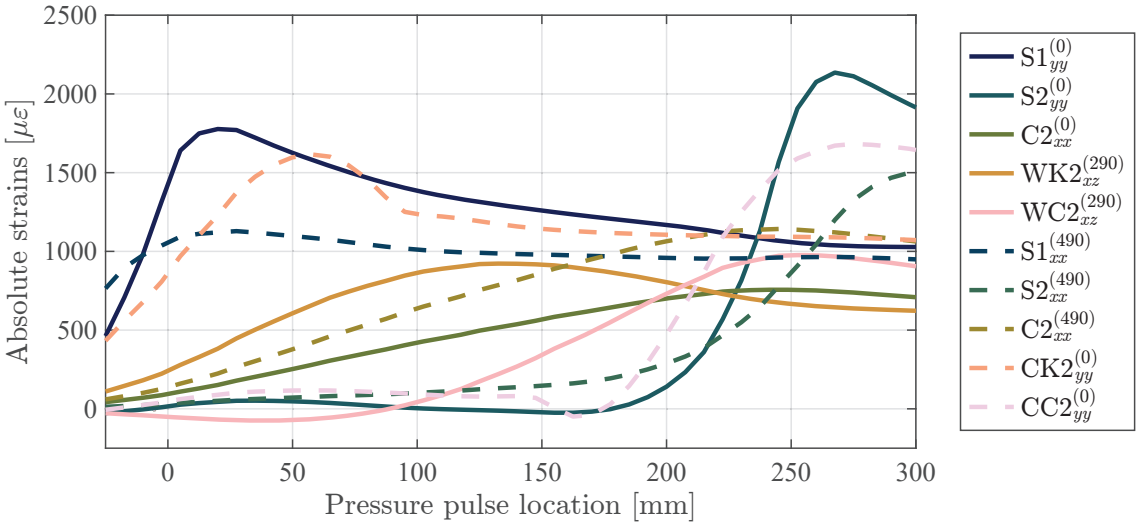

Figure 17. Critical strains of the SSCP specimen as a function of the location of the pressure pulse along the wetted surface for a 2.0 m s^{-1} quasi-static rigid impact.

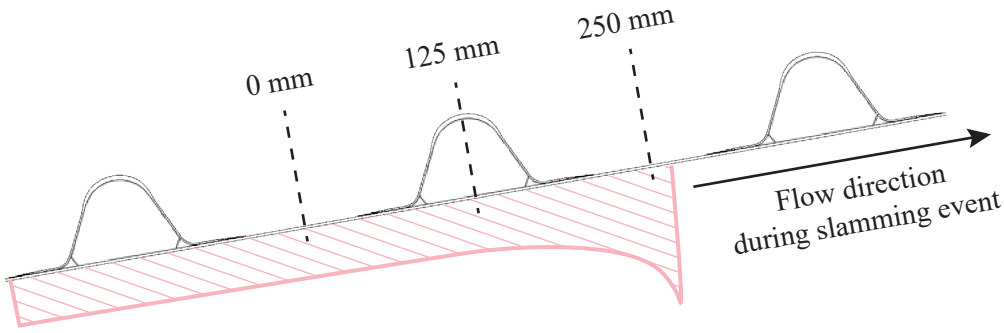

Figure 18. Location of the pressure pulse at 265 mm along the wetted surface of an SSCP.

Importantly, solving the structural response when pressure pulse was located at 245–265 mm (when the stringer was most loaded) captures the instants of peak strain for $S2^{(0)}_{xx}$, $CC2^{(0)}_{yy}$, $C^{(0)}_{xx}$, $C^{(495)}_{xx}$, and $WC2^{(290)}_{xz}$. As a rigid impact predicts chine-side skin and web strains to be larger than the keel-side, simulation of the instant when the stringer is most loaded captures the maximum overall skin, capping and web strains all at once. Improvements in computational efficiency can be made through a substructure modelling approach, where an initial simulation of a large, multi-stringer panel is carried out to obtain deformations. As deformations were found to converge faster than strains, this can be conducted using a relatively coarse mesh. Deformations from the larger model can then be applied the boundaries of a smaller model with a fine mesh to more accurately determine laminate strains.

5 CONCLUSIONS

A two-way coupled CFD-FEA analysis of a water impacting SSCP has been conducted to study the effects of uniform pressures, slamming pressures and hydroelasticity, and to determine the validity of the use of a static uniform pressure load during the design process of the outer hull panels of high-performance racing yacht. The key conclusions of this work are:

- Hydroelasticity results in a delay in the strain response. A larger delay was observed in skin regions closer to the chine, indicating that hydroelastic effects become more prominent as the impact event progresses. The delay in the capping strains in the central stringer becomes less pronounced closer to the bulkhead, with peak strains 290 mm from the midspan occurring 11%

earlier into the impact at the highest velocities tested here. Chine-side web strains exhibit a 54.7% larger delay with increased impact velocities compared to keel-side web.

- The effects of hydroelasticity, with local changes in panel deadrise angle and relative impact velocities results in a reduction in the peak strains of an SSCP. This implies that under the studied conditions, the omission of hydroelasticity during a water impact results in a naturally conservative prediction of the structural response. However, more work is required to determine is this holds true for a wider range of water impacts scenarios.
- The inertial response of a high-performance SSCP during a water impact is minimal due to the large loads and thin/lightweight construction. This implies that approximating the impact event as a quasi-static event is a reasonable approach, and results in a negligible (abit conservative) overprediction of peak strains
- Regardless of the impact velocity, peak strains are dependent on the relative location of the pressure pulse on the wetted surface of the SSCP. This indicates that the timing of peak strains is predictable for a given impact orientation.

Combining these conclusions indicates that the critical strains in the skin, capping, and web of a slamming SSCP can be determined by statically solving for a series of key instants, rather than the entire slamming event. The location and shape of the pressure distribution for a given deadrise and impact velocity can be readily obtained from an analytical solution without the need for costly hydroelastic fluid simulations. These results agree that further structural optimisation and resiliency is possible if a rigid impact analysis is incorporated into the design process, which can be achieved through quasi-statically simulating key instants of the slamming event. However, more work is required to convert the suggestions made in this paper into a form that can be easily and readily employed in a design office. The Authors are currently developing this methodology to explore the relationships between design of SSCPs (i.e. spacing, cross-sectional configuration, laminate stiffness) and their response under slamming loading conditions, to further quantify the discrepancies between the structural response of SSCPs under uniform and non-uniform out-of-plane pressure loads, and to compare the predictions against the solution methods outlined by design standards to determine their validity.

ACKNOWLEDGEMENTS

This work was funded by the University of Auckland Doctoral Scholarship, and the Lloyd's Register Foundation Small Grant —*Sg11-100252: Making an Impact: Updating Safety Standards for Small Marine Craft*— which covered all associated costs associated with this research.

REFERENCES

Allen, R. G., Jones, R. R., and Taylor, D. W. (1978). A Simplified Method for Determining Structural Design-Limit Pressures on High Performance Marine Vehicles. *AIAA/SNAME Advanced Marine Vehicles Conference*. San Diego, California, pp. 1–11.

Allen, T. (2013). Mechanics of Flexible Composite Hull Panels Subjected to Water Impacts. PhD. University of Auckland.

Allen, T. and Battley, M. (2015). Quantification of hydroelasticity in water impacts of flexible composite hull panels. *Ocean Engineering* 100, pp. 117–125. ISSN: 00298018. DOI: 10.1016/j.oceaneng.2015.04.012.

Ansys, Inc (2017). *ANSYS Fluent User's Guide*. Ansys.

Battley, M. and Allen, T. (Jan. 2012). Servo-hydraulic System for Controlled Velocity Water Impact of Marine Sandwich Panels. *Experimental Mechanics* 52.1, pp. 95–106. ISSN: 00144851. DOI: 10.1007/s11340-011-9543-7.

Battley, M., Allen, T., Pehrson, P., Stenius, I., and Rosén, A. (2009). Effects of Panel Stiffness on Slamming Responses of Composite Hull Panels. *International Conference on Composite Materials*, pp. 1–11.

Bisagni, C., Vescovini, R., and Dávila, C. G. (2011). Single-stringer Compression Specimen for the Assessment of Damage Tolerance of Postbuckling Structures. *Journal of Aircraft* 48.2, pp. 495–502. ISSN: 15333868. DOI: 10.2514/1.C031106.

Breder, J. (2005). Experimental Testing of Slamming Pressures on a Rigid Marine Panel. MA thesis. KTH Royal Institute of Technology.

Camilleri, J. (2017). Experimental and numerical investigation of slamming loads on high-speed craft including hydroelastic effects. PhD thesis. University of Southampton.

Causin, P., Gerbeau, J., and Nobile, F. (2005). Added-mass effect in the design of partitioned algorithms for fluid–structure problems. *Computer Methods in Applied Mechanics and Engineering* 194.42, pp. 4506–4527. ISSN: 0045-7825. DOI: https://doi.org/10.1016/j.cma.2004.12.005.

Celik, I. B., Ghia, U., Roache, P. J., Freitas, C. J., Coleman, H., and Raad, P. E. (2008). Procedure for Estimation and Reporting of Uncertainty Due to Discretisation in CFD Applications. *Journal of Fluids Enigineering* 130 (7), pp. 1–4.

Çengel, Y., Cimbala, J., and Turner, R. (2017). *Fundamentals of Thermal-Fluid Sciences*. Mcgraw-Hill Education.

Charca, S. and Shafiq, B. (Jan. 2011). Damage assessment due to repeated slamming of foam core sandwich composites. *Journal of Sandwich Structures and Materials* 13.1, pp. 97–109. ISSN: 10996362. DOI: 10.1177/1099636209344131.

Charca, S., Shafiq, B., and Just, F. (Sept. 2009). Repeated slamming of sandwich composite panels on water. *Journal of Sandwich Structures and Materials* 11.5, pp. 409–424. ISSN: 10996362. DOI: 10.1177/1099636209103169.

Chen, Z., Jiao, J., Wang, S., and Guedes Soares, C. (2023). CFD-FEM simulation of water entry of a wedged grillage structure into Stokes waves. *Ocean Engineering* 275, p. 114159. ISSN: 0029-8018. DOI: https://doi.org/10.1016/j.oceaneng.2023.114159.

Dassault Systemes (2016). *Abaqus Theory Guide*.

Davis, K., Schulte, M., and Uekermann, B. (2022). Enhancing Quasi-Newton Acceleration for Fluid-Structure Interaction. *Mathematical and Computational Applications* 27.3. ISSN: 2297-8747. DOI: 10.3390/mca27030040.

Fraunhofer SCAI (2023). *MpCCI 4.71-1 Documentation*. Schloss Birlinghoven 1, 53757 Sankt Augustin, Germany: Fraunhofer SCAI.

Hayward, A. T. J. (1967). Compressibility equations for liquids: a comparative study. *British Journal of Applied Physics* 18.7. DOI: 10.1088/0508-3443/18/7/312.

Heller, S. and Jasper, N. (1960). On the Structural Design of Planing Craft. *Quarterly Transactions. Royal Institute of Naval Architects (RINA)*.

Hosseinzadeh, S., Tabri, K., Hirdaris, S., and Sahk, T. (2023a). Slamming loads and responses on a non-prismatic stiffened aluminium wedge: Part I. Experimental study. *Ocean Engineering* 279, p. 114510. ISSN: 0029-8018. DOI: https://doi.org/10.1016/j.oceaneng.2023.114510.

Hosseinzadeh, S., Tabri, K., Topa, A., and Hirdaris, S. (2023b). Slamming loads and responses on a non-prismatic stiffened aluminium wedge: Part II. Numerical simulations. *Ocean Engineering* 279, p. 114309. ISSN: 0029-8018. DOI: https://doi.org/10.1016/j.oceaneng.2023.114309.

ISO (2019). *ISO 12215-5 Small craft - Hull construction and scantlings -Part 5: Design pressures for monohulls, design stresses, scantlings determination*.

Koch, M. D. (2016). Quasi-Newton Methods for Unstable Partitioned Fluid-Structure Interactions. MA thesis. Institute for Numerical Simulation, Rheinische Friedrich-Wilhelms-Universität Bonn.

Lorimer, T. and Allen, T. (Dec. 2022). Concurrent Multi-Component Optimization of Stiffened-Plate Yacht Structures. *Journal of Sailing Technology* 7.01, pp. 203–227. ISSN: 2475-370X. DOI: 10.5957/jst/2022.7.10.203.

Pearson, C. (2025). Design of High-Speed Hull Structures and Analysis of Failure Mechanics Under Dynamic Ocean Loads - Preprint. PhD thesis. University of Auckland.

Pearson, C., Battley, M., Little, J., Verdier, G., and Allen, T. (2026a). Structural characterisation and failure mechanisms of high-performance marine stringers in out-of-plane bending loads. *Composite Structures* 381, p. 120054. ISSN: 0263-8223. DOI: https://doi.org/10.1016/j.compstruct.2026.120054.

Pearson, C., de Mourgues, M., Battley, M., Michaud, V., Little, J., Verdier, G., and Allen, T. (2024). On the influence of flow-front orientation on stringer stiffened composite panels in water impacts. *Ocean Engineering* 303, p. 117797. ISSN: 0029-8018. DOI: https://doi.org/10.1016/j.oceaneng.2024.117797.

Pearson, C., Shepherd, N., Battley, M., and Allen, T. (2026b). On the development of a numerical slamming tank to replicate quasi-two-dimensional experimental water impacts. *Applied Ocean Research* 166, p. 104901. ISSN: 0141-1187. DOI: https://doi.org/10.1016/j.apor.2025.104901.

Pearson, C., Shepherd, N., Battley, M., and Allen, T. (2026c). The effects of hydroelasticity on stringer-stiffened composite panels in water impacts: An experimental study. *Ocean Engineering* 345, p. 123594. ISSN: 0029-8018. DOI: https://doi.org/10.1016/j.oceaneng.2025.123594.

Qi, L. (2018). A Study of the Buckling Behaviour of Stiffened Panels under Compression and Lateral Pressure. PhD thesis. TU Delft.

Roache, P. J. (1994). Perspective: A Method for Uniform Reporting of Grid Refinement Studies. *Journal of Fluids Engineering* 116, pp. 405–413.

Rosén, A., Garme, K., and Kuttenkeuler, J. (2007). Full-Scale Design Evaluation of the Visby Class Corvette. *Ninth International Conference on Fast Sea Transportation*. Shanghai. ISBN: 9781626239777.

Silva, G., Le Riche, R., Jerome, M., and Vautrin, A. (2009). Exact and efficient interpolation using finite elements shape functions. *European Journal of Computational Mechanics* 18, pp. 307–331.

Souppez, J.-B. R. G. (June 2018). Structural Design of High Performance Composite Sailing Yachts Under the New BS EN ISO 12215-5. *Journal of Sailing Technology* 3.01, pp. 1–18. ISSN: 2475-370X. DOI: 10.5957/jst.2018.02.

Stenius, I., Rosén, A., Battley, M., and Allen, T. (Dec. 2013). Experimental hydroelastic characterization of slamming loaded marine panels. *Ocean Engineering* 74, pp. 1–15. ISSN: 00298018. DOI: 10.1016/j.oceaneng.2013.09.007.

Tveitnes, T., Fairlie-Clarke, A. C., and Varyani, K. (Oct. 2008). An experimental investigation into the constant velocity water entry of wedge-shaped sections. *Ocean Engineering* 35.14-15, pp. 1463–1478. ISSN: 00298018. DOI: 10.1016/j.oceaneng.2008.06.012.

Vescovini, R. and Bisagni, C. (2015). Semi-analytical buckling analysis of omega stiffened panels under multi-axial loads. *Composite Structures* 120, pp. 285–299. ISSN: 02638223. DOI: 10.1016/j.compstruct.2014.10.003.

Vescovini, R., Dávila, C. G., and Bisagni, C. (Feb. 2013). Failure analysis of composite multi-stringer panels using simplified models. *Composites Part B: Engineering* 45.1, pp. 939–951. ISSN: 13598368. DOI: 10.1016/j.compositesb.2012.07.030.

Xie, H., Ren, H., Qu, S., and Tang, H. (2018). Numerical and experimental study on hydroelasticity in water-entry problem of a composite ship-hull structure. *Composite Structures* 201, pp. 942–957. ISSN: 0263-8223. DOI: https://doi.org/10.1016/j.compstruct.2018.06.030.

Yan, D., Mikkola, T., Lakshmynarayanana, A., Tödter, S., Schellin, T. E., Neugebauer, J., Moctar, O. el, and Hirdaris, S. (2022). A study into the FSI modelling of flat plate water entry and related uncertainties. *Marine Structures* 86, p. 103296. ISSN: 0951-8339. DOI: https://doi.org/10.1016/j.marstruc.2022.103296.

Zhao, R. and Faltinsen, O. M. (1993). Water entry of two-dimensional bodies. *Journal of Fluid Mechanics* 246.4, pp. 593–612. ISSN: 14697645. DOI: 10.1017/S002211209300028X.